



CHORUS

This is the accepted manuscript made available via CHORUS. The article has been published as:

Orbital quantum magnetism in spin dynamics of strongly interacting magnetic lanthanide atoms

Ming Li, Eite Tiesinga, and Svetlana Kotochigova

Phys. Rev. A **97**, 053627 — Published 31 May 2018

DOI: [10.1103/PhysRevA.97.053627](https://doi.org/10.1103/PhysRevA.97.053627)

Orbital quantum magnetism in spin dynamics of strongly interacting magnetic lanthanide atoms

Ming Li^a, Eite Tiesinga^b and Svetlana Kotochigova^{a*}

*Corresponding author. Email: skotoch@temple.edu

^a*Department of Physics, Temple University, Philadelphia, PA 19122-6082, USA*

^b*Joint Quantum Institute and Joint Center for Quantum Information and Computer Science, National Institute of Standards and Technology and University of Maryland, Gaithersburg MD 20899, USA*

Laser cooled lanthanide atoms are ideal candidates with which to study strong and unconventional quantum magnetism with exotic phases. Here, we use state-of-the-art closed-coupling simulations to model quantum magnetism for pairs of ultracold spin-6 erbium lanthanide atoms placed in a deep optical lattice. In contrast to the widely used single-channel Hubbard model description of atoms and molecules in an optical lattice, we focus on the single-site *multi-channel* spin evolution due to spin-dependent contact, anisotropic van der Waals, and dipolar forces. This has allowed us to identify the leading mechanism, *orbital anisotropy*, that governs molecular spin dynamics among erbium atoms. The large magnetic moment and combined orbital angular momentum of the 4f-shell electrons are responsible for these strong anisotropic interactions and unconventional quantum magnetism. *Multi-channel* simulations of magnetic Cr atoms under similar trapping conditions show that their spin-evolution is controlled by spin-dependent contact interactions that are distinct in nature from the orbital anisotropy in Er. The role of an external magnetic field and the aspect ratio of the lattice site on spin dynamics is also investigated.

I. INTRODUCTION

Magnetic moments of atoms and molecules originate from their electrons *intrinsic* spin as well as their orbital angular momentum. In solids the orbital component of the magnetic dipole moment revolutionized spintronics research and led to a novel branch of electronics, orbitronics [1]. The orbital magnetic moment is large in materials containing partially filled inner shell atoms. The distinguishing feature of such atoms is the extremely large anisotropy in their interactions. This orbital anisotropy is the crucial element in various scientific applications and magnetic technology [2–4].

Inspired by the role of orbital anisotropy in magnetic solids and to deepen our knowledge of quantum magnetism, we study orbital anisotropy at the elementary level by capturing the behavior of strongly-interacting magnetic lanthanide atoms in an optical lattice site. In particular, we simulate the time-dependent *multi-channel* spin-exchange dynamics of pairs of interacting erbium atoms in sites of a deep three-dimensional optical lattice with negligible atomic tunneling between lattice sites.

Theoretical spin models have a long established role as useful tools for understanding interactions in magnetic materials. Recently, researchers demonstrated that laser-cooled ultracold atoms and molecules in optical lattices are a nearly perfect realization of these models with control of the local spin state and spin-coupling strength [5–15]. However, most of the microscopic implementation of spin models has focussed on atoms with zero orbital angular momentum and often based on a single-state (Fermi- or Bose-) Hubbard model description [16, 17].

The limitation of simplified Hubbard models essentially holds true for optical lattices filled with magnetic lanthanide atoms that have open electronic 4f-shells and

possess a large unquenched orbital angular momentum. These atoms are now emerging as a promising platform for the investigation of high-spin quantum magnetism. Theoretical simulations of ultracold lanthanide atoms in an optical lattice is a difficult task that requires multi-channel analyses of interactions and correlations.

Although quantum many-body effects have been observed and studied with quantum gases of lanthanide atoms [15, 18–21], the on-lattice-site spin dynamics of highly magnetic atoms remains not fully understood as it requires a precise knowledge of the two-body interactions.

We, first, focus on single-site *multi-channel* spin evolution due to spin-dependent contact, anisotropic van-der-Waals, and dipolar forces. Then, we go beyond the one-site model in order to account for coupling between our atom pair and other (doubly-)occupied lattice sites and find a slow damping of the local spin oscillations. In our Mott insulator regime, the single-site quasi-molecule is surrounded by atom pairs in neighboring sites. This only permits the magnetic dipole-dipole coupling between the atom pairs justified by studies [8, 22] showing that for short-range interactions between atoms in neighboring lattice sites is orders of magnitude weaker than the dipole-dipole interaction.

Dipole-dipole interaction induced quantum magnetism was pioneered in experiments of Laburthe-Tolra’s group [23]. The authors used magnetic chromium atoms with their three units of angular momenta and demonstrated the most-dramatic spin oscillations observed to date. These oscillations resulted from the strong coupling between the spins, both from isotropic spin-dependent on-site contact interactions and between-site magnetic dipole-dipole interactions.

We have shown here that the orbital-induced molecu-

lar anisotropy, absent in alkali-metal and chromium collisions, is much stronger in interactions of lanthanide atoms than that of the magnetic dipole-dipole interaction at interatomic separations smaller than $200a_0$, where a_0 is the Bohr radius. At shorter separations the strength of this anisotropy for Dy and Er atoms is about 10% that of the spin-independent isotropic interaction.

II. SPIN-CHANGING COLLISIONS OF LANTHANIDE ATOMS

To shed light on these spin oscillations we simulate spin-changing collisions in individual doubly-occupied lattice sites in the presence of a magnetic field \vec{B} . The single-site lattice potential is well approximated by a cylindrically-symmetric harmonic trap and then the Hamiltonian for the relative motion of two ground-state bosonic lanthanide atoms is $H_{\text{rel}} = H_0 + U$, where

$$H_0 = \vec{p}^2/(2\mu) + \mu(\omega_\rho^2 \rho^2 + \omega_z^2 z^2)/2 + H_Z$$

with relative momentum \vec{p} , relative coordinate $\vec{r} = (r, \theta, \varphi) = (\rho, \phi, z)$ between the atoms in spherical and cylindrical coordinates, respectively, and reduced mass μ . Moreover, ω_ρ and ω_z are trapping frequencies and $H_Z = g\mu_B(\vec{j}_a + \vec{j}_b) \cdot \vec{B}$ is the Zeeman Hamiltonian with atomic g-factor g and Bohr magneton μ_B . (Here and throughout, we use dimensionless angular momenta, i.e. \vec{j}/\hbar is implied when we write \vec{j} with reduced Planck constant \hbar . For angular momentum algebra and notation we follow Ref. [24].) Zeeman states $|j_a, m_a\rangle|j_b, m_b\rangle$ are eigen states of H_Z , where \vec{j}_α is the total atomic angular momentum of atom $\alpha = a$ or b and m_α is its projection along \vec{B} . Here, we have assumed that the harmonic trap is the same for all atomic states and that the B -field direction is along the axial or z direction of the trap. The lasers generating the optical lattice often induce small tensor light shifts proportional to $(m_{a,b})^2$ [23]. We have omitted this effect. Finally, we define the ‘‘isotropic’’ trap frequency ω via $\omega^2 = (\omega_z^2 + 2\omega_\rho^2)/3$.

The Hamiltonian term U describes the molecular interactions. It contains an isotropic contribution $U^{\text{iso}}(r)$ that only depends on r as well as an anisotropic contribution $U^{\text{aniso}}(\vec{r})$ that also depends on the orientation of the internuclear axis. In fact, we have $U^{\text{iso}}(r) = V_0(r) + V^{\text{jj}}(r)\vec{j}_a \cdot \vec{j}_b + \dots$, where for $r \rightarrow \infty$ the angular-momentum independent $V_0(r) \rightarrow -C_6/r^6$ with dispersion coefficient $C_6 = 1723E_h a_0^6$ for Er_2 [25, 26]. For small r the potential $V_0(r)$ has a repulsive wall and an attractive well with depth $D_e/(hc) \approx 790 \text{ cm}^{-1}$. We use $V^{\text{jj}}(r) = -c_6^{\text{jj}}/r^6$ for all r with $c_6^{\text{jj}} = -0.1718E_h a_0^6$. Furthermore, $U^{\text{aniso}}(\vec{r}) = U^{\text{orb}}(\vec{r}) + U^{\text{dip}}(\vec{r})$ with

$$U^{\text{orb}}(\vec{r}) = V^{\text{orb}}(r) \sum_{i=a,b} \frac{3(\hat{r} \cdot \vec{j}_i)(\hat{r} \cdot \vec{j}_i) - \vec{j}_i \cdot \vec{j}_i}{\sqrt{6}} + \dots,$$

and

$$U^{\text{dip}}(\vec{r}) = -\frac{\mu_0(g\mu_B)^2}{4\pi} \frac{3(\hat{r} \cdot \vec{j}_a)(\hat{r} \cdot \vec{j}_b) - \vec{j}_a \cdot \vec{j}_b}{r^3}$$

is the magnetic dipole-dipole interaction. We use $V^{\text{orb}}(r) = -c_6^{\text{orb}}/r^6$ for all r with $c_6^{\text{orb}} = -1.904E_h a_0^6$. Finally, E_h is the Hartree energy, h is Planck’s constant, c is the speed of light in vacuum, and μ_0 is the magnetic constant.

The dispersion coefficient C_6 is the largest coefficient by far, making the van-der-Waals length $R_6 = \sqrt[4]{2\mu C_6/\hbar^2}$ the natural length scale for the dispersive interactions. The contribution to $U^{\text{orb}}(\vec{r})$ with strength $V^{\text{orb}}(r)$ is the strongest anisotropic orbital interaction. It couples the angular momentum of each atom to the rotation of the molecule. Anisotropic terms entangle spin and orbital degrees of freedom and play a similar role as spin-orbit couplings induced by synthetic magnetic fields [27, 28]. The short-range shape of $V_0(r)$ and those for $V^{\text{jj}}(r)$ and $V^{\text{orb}}(r)$ are known from the combine experimental measurements and *ab initio* calculations [26, 29]. All results unless otherwise noted have been performed with short-range potentials that reproduce the experimentally determined scattering length of $137a_0$ for the lowest Zeeman sublevel near zero magnetic field [30]. The consequences of the uncertainties in the potentials will be discussed later on.

For future reference and following the convention in the literature the natural length scale for the magnetic dipole-dipole interaction is $a_{\text{dd}} = (1/3) \times 2\mu C_3/\hbar^2$ with coefficient $C_3 = \mu_0(g\mu_B j)^2/(4\pi)$, where $j = 6$ and $g = 1.16381$ for Er.

The Hamiltonian H_{rel} commutes with J_z and only couples even or odd values of ℓ , the relative orbital angular momentum or partial wave. Here, J_z is the z projection of the total angular momentum $\vec{J} = \vec{\ell} + \vec{j}$ with $\vec{j} = \vec{j}_a + \vec{j}_b$. For $B = 0$ H_{rel} also commutes with J^2 . Hence, eigenstates $|i, M\rangle$ of H_{rel} with energy $E_{i,M}$ are labeled by projection quantum number M . These eigen pairs have been computed in the basis

$$|(j_a j_b) j \ell; JM\rangle \equiv \sum_{m_j m} \langle j \ell m_j m | JM \rangle |(j_a j_b) j m_j\rangle Y_{\ell m}(\theta, \varphi)$$

with $|(j_a j_b) j m_j\rangle = \sum_{m_a m_b} \langle j_a j_b m_a m_b | j m_j \rangle |j_a m_a\rangle |j_b m_b\rangle$, spherical harmonic function $Y_{\ell m}(\theta, \varphi)$, and $\langle j_1 j_2 m_1 m_2 | j m \rangle$ are Clebsch-Gordan coefficients. For our bosonic system only basis states with even $\ell + j$ exist. We use a discrete variable representation (DVR) [31, 32] to represent the radial coordinate r . The largest r value is a few times the largest of the harmonic oscillator lengths $\sqrt{\hbar/(\mu\omega_{\rho,z})}$ with $\hbar = h/(2\pi)$ and for typical traps $R_6 \ll \sqrt{\hbar/(\mu\omega_{\rho,z})}$. We further characterize the eigen states by computing overlap amplitudes with those at different B field values. In particular, overlaps with $B = 0$ eigenstates give us approximate J value. The expectation value of operators j^2 and ℓ^2 are also computed.

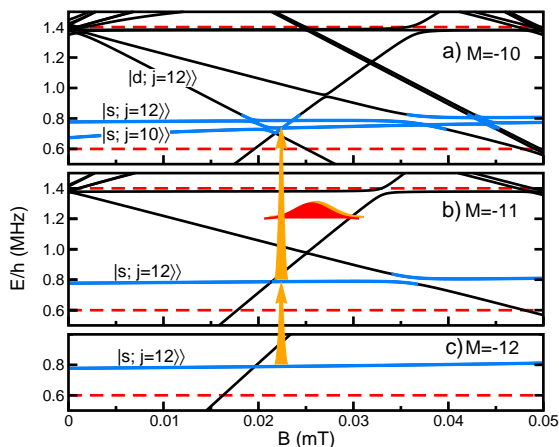


FIG. 1. Near-threshold energy levels of the relative motion of two harmonically trapped and interacting ^{168}Er atoms with $M = -10, -11$, and -12 in panel a), b), and c), respectively. The trap is isotropic with $\omega/(2\pi) = 0.4$ MHz. In the three panels the zero of energy corresponds to the Zeeman energy of two atoms at rest with $m_a + m_b = -10, -11$, and -12 , respectively. Dashed red lines correspond to the first and second harmonic-oscillator levels with energies $(3/2)\hbar\omega$ and $(7/2)\hbar\omega$, respectively. Blue curves indicate the energy levels that are involved in the spin-changing oscillations. Some of the eigenstates have been labeled by their dominant ℓ and j contribution. Orange arrows (not to scale) and a red rf pulse indicate single-color two-photon rf transitions that initiate the spin oscillations starting from two atoms in the $|6, -6\rangle$ state.

III. RESULTS AND DISCUSSION

A. Eigenstates in an isotropic lattice site

Figure 1 shows even- ℓ , above-threshold $^{168}\text{Er}_2$ energy levels in an isotropic harmonic trap and $M = -12, -11$, or -10 as functions of B up to 0.05 mT. The energies of two harmonic oscillator levels are also shown. The energetically-lowest is an $\ell = 0$ or s -wave state with energy $(3/2)\hbar\omega$; the second is degenerate with one s - and multiple $\ell = 2$, d -wave states and $(7/2)\hbar\omega$. In each panel one or two eigenstates with energies that run nearly parallel with these oscillator energies exist. In fact, their energy, just above $(3/2)\hbar\omega$, indicates a repulsive effective atom-atom interaction [33, 34]. For our weak B fields and *away* from avoided crossings their wavefunctions are well described by or are correlated to a single $J = 10$ or 12 zero- B eigenstate. Further, they have an s -wave dominated spatial function, $j \approx J$, and $m_j \approx M$. These eigenstates will be labeled by $|s; jm_j\rangle$ away from avoided crossings.

A single bound state with $E < 0$ when $B = 0$ and a negative magnetic moment can be inferred in each panel of Fig. 1. It avoids with several trap states when $B > 0.015$ mT and has mixed g - and i -wave character away from avoided crossings. In free space this bound state would induce a d -wave Feshbach resonance near $B = 6$

μT (not shown).

Figure 1 also shows eigenstates with energies close to $E = (7/2)\hbar\omega$ when $B = 0$. For $B > 2 \mu\text{T}$ and away from avoided crossings, these states have d -wave character, are well described by a single j, m_j pair, and have a magnetic moment, $-dE_{i,M}/dB$, that is an integer multiple of $g\mu_B$. D -wave states with a positive magnetic moment in the figure have avoided crossings with s -wave states $|s; jm_j\rangle$ and play an important role in our analysis of spin oscillations. We focus on the three-state avoided crossing in panel a) near $B = 0.020$ mT, where the corresponding d -wave state has $j = 12$ and $m_j = -12$ and will be labeled by $|d; jm_j\rangle$. Close to the avoided crossings the three eigenstates of H_{rel} are superpositions of the B -independent $|s; jm_j\rangle$ and $|d; jm_j\rangle$ states. The mixing coefficients follow from the overlap amplitudes with eigenstates well away from the avoided crossing. In other words $|i, M = -10\rangle = \sum_k U_{i,k}(B) |k\rangle$ with $k = \{s; 10, -10\}, \{s; 12, -10\}$, and $\{d; 12, -12\}$ and $U(B)$ is a B -dependent 3×3 unitary matrix.

Finally, Fig. 1 shows the rf pulse that initiates spin oscillations. We choose a non-zero B field and start in $|s; 12 -12\rangle$ with $M = -12$ in panel c). After the pulse, via near-resonant intermediate states with $M = -11$, the atom pair is in a superposition of two or three eigenstates with $M = -10$. The precise superposition depends on experimental details such as carrier frequency, polarization and pulse shape. We, however, can use the following observations. The initial $|s; 12 -12\rangle$ state can also be expressed as the uncoupled product state $|6, -6\rangle|6, -6\rangle$ independent of B . As rf photons only induce transitions in atoms (and not couple to $\vec{\ell}$ of the atom pair), the absorption of one photon by each atom leads to the product s -wave state $|6, -5\rangle|6, -5\rangle$, neglecting changes to the spatial wavefunction of the atoms. To prevent population in atomic Zeeman levels with $m_{a,b} > -5$ we follow Ref. [23] and assume that light shifts induced by optical photons briefly break the resonant condition to such states.

The s -wave $|6, -5\rangle|6, -5\rangle$ state then evolves under the molecular Hamiltonian. It is therefore convenient to express this state in terms of $M = -10$ eigenstates. First, by coupling the atomic spins to \vec{j} we note $|6, -5\rangle|6, -5\rangle \rightarrow c_{10}|s; 10, -10\rangle + c_{12}|s; 12, -10\rangle$, where $c_j = \langle 66 -5 -5 | j -10 \rangle$ and each $|k\rangle$ is a superposition of three eigenstates $|i, M = -10\rangle$ as given by the inverse of $U(B)$. After free evolution for time t we measure the population of remaining in the initial state.

B. Anisotropic harmonic traps

The lattice laser beams along the independent spatial directions do not need to have the same intensity and thus the potential for a lattice site can be anisotropic. This gives us a means to extract further information about the anisotropic molecular interaction potentials. A first such experiment for Er provided evidence of the orientational dependence due to the intra-site magnetic

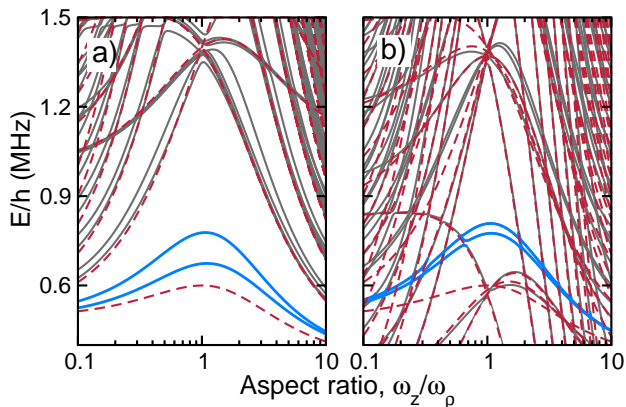


FIG. 2. Near-threshold energy levels of $^{168}\text{Er}_2$ with $M = -10$ in an anisotropic harmonic trap as a function of trap aspect ratio ω_z/ω_ρ at fixed $\omega/(2\pi) = 0.4$ MHz for $B = 0.1 \mu\text{T}$ and 0.05 mT in panels a) and b), respectively. The red dashed lines correspond to non-interacting levels. Blue lines are relevant for spin-oscillation experiments. The zero of energy in a panel is that of two free atoms at rest with $m_a + m_b = -10$ at the corresponding B field.

dipole-dipole interactions on the particle-hole excitation frequency in the doubly-occupied Mott state [30].

Figure 2 shows the near-threshold energy $M = -10$ levels in an anisotropic harmonic trap as a function of trap aspect ratio ω_z/ω_ρ at fixed $\omega/(2\pi) = 0.4$ MHz for two magnetic field strengths. Dashed lines correspond to non-interacting levels, including only the harmonic trap and Zeeman energies. For $\omega_z/\omega_\rho \rightarrow 0$ and ∞ the trap is quasi-1D and quasi-2D, respectively. Energy levels involved in spin-oscillations are highlighted in blue and for finite B their avoided crossings with other states can be studied.

C. Spin-oscillations

Following Refs. [25, 26, 30], we prepare ground-state spin-6 erbium atom pairs in the energetically-lowest vibrational state of a lattice site and Zeeman sublevel $|j_a, m_a\rangle = |6, -6\rangle$, where j_a and m_a are the atomic angular momentum and its projection along an applied magnetic field, respectively. To initiate spin dynamics we transfer each atom to Zeeman sublevel $|6, -5\rangle$ with a short rf pulse. We single out this pair state among the many internal hyperfine states, due to its ability to collisionally evolve into the $|6, -6\rangle + |6, -4\rangle$ molecular state. We then use the spin-oscillation frequency of the atomic populations to extract the energy splitting between $|6, -5\rangle + |6, -5\rangle$ and $|6, -6\rangle + |6, -4\rangle$. This magnetic-field dependent splitting is, unlike for alkali-metal and chromium atoms, due to strong orbital anisotropy in interactions between the atoms.

Figures 3a), b), and d) show our predicted $|6, -5\rangle$ population as a function of time after the short rf pulse for

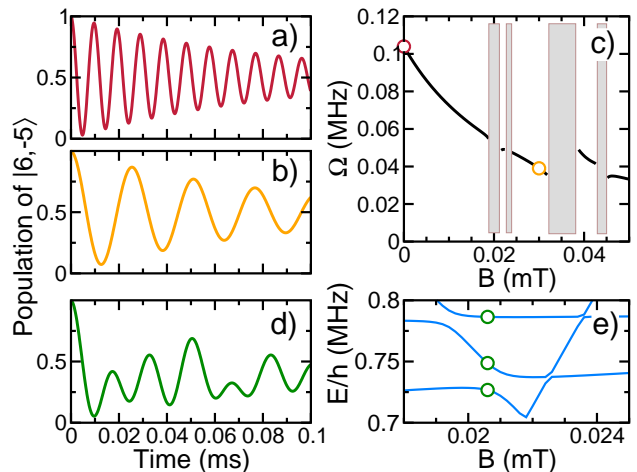


FIG. 3. Spin population dynamics of ^{168}Er in an isotropic trap with $\omega/(2\pi) = 0.4$ MHz. Panels a) and b) show sinusoidal time traces of the population in $|6, -5\rangle$ for $B = 0.1 \mu\text{T}$ and 0.03 mT, respectively. Panel c) shows the spin-oscillation frequency as a function of B with blocked out field regions (gray bands) where the oscillations are not sinusoidal. The two open circles correspond to the field values shown in panels a) and b). A complex oscillation pattern for $B = 0.0206$ mT, located in one of the banded regions, is shown in panel d). Panel e) shows the corresponding avoided crossing between the three populated energy levels. We assume a slow damping rate of $\gamma = 1.2 \cdot 10^4 \text{ s}^{-1}$. Its origin is discussed in the text.

three characteristic, but small B . The population is seen to oscillate. Those in panels a) and b) are single sinusoids with a frequency $\Omega(B)$ and reflect the fact that only two $|i, M = -10\rangle$ are populated by the pulse. We find that these states to good approximation are labeled by diabatic states $|\ell; j, m\rangle = |s; 10, -10\rangle$ and $|s; 12, -10\rangle$, where the s corresponds to $\ell = 0$, s -wave partial wave scattering and \vec{j} is the sum of the two atomic angular momenta (m is its projection). Figure 3c) shows that the frequency Ω is a sharply decreasing function of B .

In the banded regions of Fig. 3c) avoided crossings between three states occur and the spin oscillations have multiple periodicities. An example from near $B = 0.02$ mT is shown in panel d) together with a blowup of the relevant populated energy levels in panel e). The third state away from this avoided crossing is characterized by $|d; 12, -12\rangle$ with an energy that decreases with B and a large d -wave character. Near the avoided crossing eigenstates are superpositions of the three diabatic states $|k\rangle = |s; 10, -10\rangle$, $|s; 12, -10\rangle$ and $|d; 12, -12\rangle$. See Supplemental Material for more details. Neither the B -dependence of $\Omega(B)$ nor the presence of avoided crossings can be observed in atomic chromium and both are solely the consequence of the anisotropic dispersive interactions in magnetic lanthanides and form two important results of this article.

In an experiment thousands of simultaneous spin-

oscillations occur, one in each site of a D -dimensional optical lattice. Atom pairs in *different* lattices sites are coupled by magnetic dipole-dipole interactions. This leads to dephasing of the intra-site spin oscillation. Here, we estimate the timescale involved. The inter-site dipolar strength for a typical lattice period $\delta\lambda$ between 250 nm and 500 nm is an order of magnitude smaller than the energy spacings between the local $|s; j, m_j\rangle$ and $|d; j, m_j\rangle$ states. In principle, this dipole-dipole interaction can change di-atomic projection quantum numbers j and m_j . We, however, focus on couplings that are superelastic and ignore exchange processes. That is, transitions that leave j and the sum of the Zeeman energies unchanged, i.e. $|s; j_p m_p\rangle_p |s; j_q m_q\rangle_q \longleftrightarrow |s; j_p m_p + 1\rangle_p |s; j_q m_q - 1\rangle_q$ etc., where the subscripts p and q on the kets indicate different lattice sites. For N unit cells and focusing on states $|s; j, m_j\rangle_p$ of a single j this leads to $\approx (2j + 1)^N$ spin configurations when $N \gg 2j + 1$ and with nonuniformly-distributed eigenenergies that span an energy interval of order $2D \times \mu_0 / (4\pi) \times (g\mu_B j)^2 / \delta\lambda^3 \equiv \Delta$ accounting for nearest-neighbor coupling only. Here, g is the atomic g-factor, μ_B is the Bohr magneton, and μ_0 is the magnetic constant. For Er_2 , $\Delta/h = D \times 320$ Hz with $j = 12$ and $\delta\lambda = 250$ nm and Planck constant h . The value Δ is a lower bound for the energy span.

We then simulate the intra-site spin-evolution in the presence of these super-elastic dipolar processes with di-atoms in other sites with a master equation for the reduced density matrix $\rho_{kk'}(t)$ with up to three di-atomic basis states $|k\rangle$ and Lindblad operators $L_k = \sqrt{\gamma_k}|k\rangle\langle\langle k|$ [35] that damp coherences but not populations at rate $\gamma_k = 2\pi\eta_k\Delta/h$ with dimensionless parameters η_k of the order unity. Figures 3a), b), and d) show this dephasing assuming $\gamma_k = \gamma = 1.2 \cdot 10^4$ s $^{-1}$ for all k (i. e. $\eta_k = 2$ and $D = 3$). For $t \rightarrow \infty$ the overlap with the initial state approaches $|c_{j=10}|^4 + |c_{j=12}|^4 \approx 0.50$ for panels a) and b) and to a value that depends on the precise mixing of the three diabatic states for panel d).

D. Distribution of spin-oscillation frequencies

The short-range shapes of the Er interaction potentials have significant uncertainties even when taking into account of the $137a_0$ scattering length of the $|6, -6\rangle$ state. This modifies the expected spin-oscillation frequencies. We characterize the distribution of the spin-oscillation frequency by changing the depth of the isotropic and spin-independent $V_0(r)$ over a small range, such that its number of s -wave bound states changes by one, while keeping its long-range dispersion coefficient fixed. The nominal number of bound states is 72, much larger than one, and based on quantum-defect theory [36] we can assume that each depth within this range is equally likely.

Figure 4a) shows the distribution of oscillation frequencies $\Omega = |E_{i,M} - E_{i',M}|/h$ at $B = 0.1$ μT away from avoided crossings assuming an isotropic harmonic trap. Here, the eigenstates are $|i, M = -10\rangle \approx |s; 10, -10\rangle$

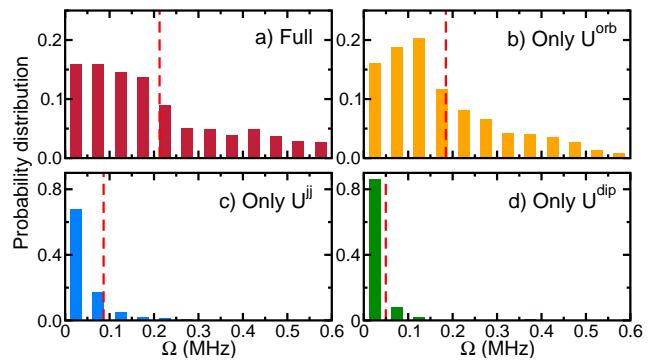


FIG. 4. Probability distributions of the $M = -10$ spin-oscillation frequency Ω showing the role of anisotropic interactions in ^{168}Er . Data is for an isotropic trap with $\omega/2\pi = 0.4$ MHz and $B = 0.1$ μT . Panels a), b), c), and d) show distributions for the full interaction potential U , $U \rightarrow V_0(r) + V^{\text{orb}}(\vec{r})$, $U \rightarrow V_0(r) + V^{\text{ij}}(r)$, and $U \rightarrow V_0(r) + V^{\text{dip}}(\vec{r})$, respectively. In each panel the mean spin-oscillation frequency is indicated by a vertical dashed line.

and $|i', M = -10\rangle \approx |s; 12, -10\rangle$. (Few of the realizations show evidence of mixing with other states.) The distribution is broad and peaked at zero frequency. Its mean frequency is $\approx 0.5\hbar\omega$ and should be compared to the $2\hbar\omega$ spacing between the harmonic levels.

We have also computed the distribution for Hamiltonians, where one or more parts of U have been turned off. In particular, Fig. 4b) shows the distribution for the case where U is replaced by $V_0(r)$ and the term proportional to $V^{\text{orb}}(\vec{r})$, while Figs. 4c) and d) show that for $U \rightarrow V_0(r) + V^{\text{ij}}(r)$ and $U \rightarrow V_0(r) + V^{\text{dip}}(\vec{r})$, respectively. The distribution in panel b) is about as broad as that in panel a) indicating that the anisotropic dispersion of $U^{\text{orb}}(\vec{r})$ is the most important factor in determining the distribution for the full U , even though the precise distribution has noticeably changed. In panel b) smaller and larger splittings are now suppressed relative to those near the mean. In panel c) with only isotropic spin-spin interactions and panel d) with only the magnetic dipole-dipole interaction coupling spins and orbital angular momenta the distributions are highly localized.

E. Comparing spin dynamics of magnetic Er and Cr

One of the most-studied ultracold magnetic atom is chromium with its magnetic moment of $6\mu_B$ and spin $s = 3$ [23, 37–41]. This moment is only slightly smaller than that of Er, $\approx 7\mu_B$. The dipolar parameter $\epsilon_{\text{dd}} = a_{\text{dd}}/a$ for these atoms, however, is very different. Here, dipolar length $a_{\text{dd}} = (1/3) \times 2\mu(g\mu_B j)^2 \mu_0 / (4\pi\hbar^2)$, a is a relevant s -wave scattering length, and μ is the reduced mass. In fact, ϵ_{dd} is 0.16 for ^{52}Cr [39] and near two for ^{168}Er [15] for the $|6, -6\rangle$ Zeeman level due to the large difference in their mass. Another distinction is their

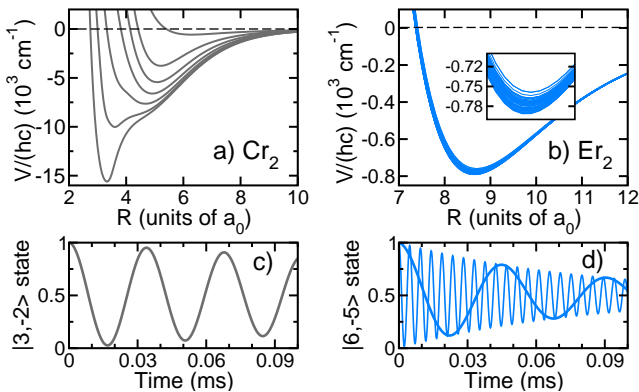


FIG. 5. Ground-state adiabatic potentials of Cr_2 and Er_2 and a comparison of their spin evolution. Panel a) shows the seven $^{2S+1}\Sigma^+$ BO potentials of Cr_2 as functions of separation r calculated in Ref. [42]. Panel b) shows the forty-nine gerade potentials of Er_2 with $\Omega = 0, \dots, 12$. Panels c) and d) show the population evolution of the $|3, -2\rangle$ and $|6, -5\rangle$ states of Cr and Er atoms at $B = 0.1 \mu\text{T}$, respectively. The solid and dashed curves in panel d) are for the full interaction potential and a potential that only includes the isotropic interactions, respectively. Damping is due to dephasing from dipolar interactions with atoms in neighboring lattice sites. The lattice geometry is the same for both atomic species and as in Fig. 3.

orbital electronic structure. Chromium has a $^7\text{S}_3$ ground state and no orbital anisotropy, whereas erbium has a $^3\text{H}_6$ ground state and a large orbital anisotropy.

Quantum magnetism of pairs of Cr atoms in a lattice site was investigated in Refs. [23, 41]. Cr atoms were prepared in the $|s, m_s\rangle = |3, -3\rangle$ state and spin dynamics was initiated by transfer into the $|3, -2\rangle$ state. Then the quasi-molecular state $|3, -2\rangle + |3, -2\rangle$ evolves into $|3, -3\rangle + |3, -1\rangle$ state and back. The energy difference between these states is due to molecular interactions.

The potential operator U for Cr_2 only contains isotropic interactions except for the magnetic dipole-dipole interaction. These isotropic potentials can be represented as a sum of tensor operators, $U^{\text{iso}}(r) = V_0(r) + V_1(r)\vec{s}_a \cdot \vec{s}_b + V_2(r)T_2(\vec{s}_a, \vec{s}_a) \cdot T_2(\vec{s}_b, \vec{s}_b) + \dots$ for atoms a and b , where $V_0(r)$ has an attractive well and a dispersion potential with $C_6 = 733E_h a_0^6$ for $r \rightarrow \infty$ [38] and $V_1(r)$ is the exchange potential proportional to $r^\gamma e^{-\kappa r}$ for $r \rightarrow \infty$. The non-negligible $V_2(r)$ is the strength of a second spin-dependent contribution. It and any other additional operator also decrease exponentially with r . The rank-2 tensor $T_2(\vec{s}_a, \vec{s}_b)$ is constructed from angular momenta \vec{s}_a and \vec{s}_b .

For Cr_2 the tensor description of U is equivalent to a description in terms of Born-Oppenheimer (BO) or adiabatic potentials, labeled $^{2S+1}\Sigma_{g/u}^+$ with $\vec{S} = \vec{s}_a + \vec{s}_b$ and $S = 0, 1, \dots, 6$ (Even and odd spin S corresponds to *gerade*(g) and *ungerade*(u) symmetry, respectively.) They were computed in Ref. [42] and reproduced in Fig. 5a). The complex relationship between the BO potentials indicates that $V_{q>0}(r)$ are on the order of $V_q/(hc) = 10^3$

cm^{-1} for $r < 6a_0$. Figure 5b) shows the equivalent graph for two Er atoms as obtained by diagonalizing our U at each r with \vec{r} aligned along the internuclear axis. The potentials have depths $D/(hc)$ between 750 cm^{-1} and 790 cm^{-1} at the equilibrium separation, where the splittings are mainly due to the anisotropic interaction proportional to $V^{\text{orb}}(r)$. Visually, the adiabatic potentials of the two species are very distinct. The crucial physical distinction, however, lies in the origin of the splittings between the potentials, i.e. isotropic versus anisotropic interactions.

We find it convenient to simulate the spin dynamics of Cr by replacing the $V_q(r)$ by delta-function or contact potentials $4\pi(\hbar^2/2\mu)\mathcal{A}_q\delta(\vec{r})\partial/\partial r$ for $q = 0, 1$ and 2 , with fitted lengths \mathcal{A}_q such that the contact model reproduces the measured scattering lengths of the BO potentials. We used $\mathcal{A}_0 = 60.6a_0$, $\mathcal{A}_1 = 6.73a_0$ and $\mathcal{A}_2 = -0.243a_0$ leading to the measured scattering lengths of $-7(20)a_0$, $58(6)a_0$, and $112(14)a_0$ for the $S = 2, 4$, and 6 potentials, respectively [38]. (The numbers in parenthesis are the quoted uncertainties. The scattering length for the $^1\Sigma_g^+$ potential is not known. The \mathcal{A}_q will change once this scattering length is determined.)

Figures 5c) and d) compare the spin oscillations for a pair of Cr and Er atoms for the same lattice geometry and $B = 0.1 \mu\text{T}$, respectively. The eigen energies of a Cr pair in an isotropic harmonic trap interacting via the delta function potentials are found with the help of the non-perturbative analytical solutions obtained in Ref. [33]. The spin evolution for Cr is solely due to the isotropic spin-spin interactions proportional to lengths \mathcal{A}_1 and \mathcal{A}_2 and are independent of B . Two time traces for Er are shown corresponding to the full U and one where only the isotropic interactions are included. We see that the oscillation period is slower when the anisotropic interactions are excluded and the behavior is much more alike to that of a Cr pair. The curves in panels c) and d) also include an estimate of dephasing due to atom pairs in neighboring lattice sites again using a lattice spacing of 250 nm . Dephasing of a chromium-pair is only 25% smaller than that of an erbium-pair due to the slightly-smaller magnetic moment of Cr.

IV. CONCLUSION

We have presented simulations that give valuable insight into the interactions of lanthanide-based quantum systems with periodic arrays or lattices containing atom pairs in each lattice site. As our atoms carry a spin that is much larger than that of spin-1/2 electrons in magnetic solid-state materials, this might result in a wealth of novel quantum magnetic phases. The ultimate goal of any Atomic, Molecular and Optical implementation of quantum magnetism is to develop a controllable environment in which to simulate materials with new and advanced functionality.

In spite of the successes of previous analyses of quan-

tum simulations with (magnetic) atoms in optical lattices [43], simplified representations with atoms as point particles and point dipoles can not always be applied to magnetic lanthanide atoms. Important information about the electron orbital structure within the constituent atoms is lost.

In the current study the orbital anisotropy of magnetic-lanthanide electron configurations is properly treated in the interactions between Er atoms in optical lattice sites and is used to describe and predict spin-oscillation dynamics. We illuminated the role of orbital anisotropy in this spin dynamics as well as studied the interplay between the molecular anisotropy and the geometry of the

lattice site potential. The interactions lift the energy-degeneracies of different spin orientations, which, in turn, leads to spin oscillations.

V. ACKNOWLEDGMENTS

Work at Temple University is supported by the AFOSR Grant No. FA9550-14-1-0321, the ARO-MURI Grants No. W911NF-14-1-0378, ARO Grant No. W911NF-17-1-0563, and the NSF Grant No. PHY-1619788. The work at the JQI is supported by NSF Grant No. PHY-1506343.

-
- [1] D. Go, J.-P. Hanke, P. M. Buhl, F. Freimuth, G. Bihlmayer, H.-W. Lee, Y. Mokrousov, and S. Blügel, *Scientific Reports* **7**, 46742 (2017).
- [2] B. A. Bernevig, T. L. Hughes, and S.-C. Zhang, *Phys. Rev. Lett.* **95**, 066601 (2005).
- [3] H. Kontani, T. Tanaka, D. S. Hirashima, K. Yamada, and J. Inoue, *Phys. Rev. Lett.* **100**, 096601 (2008).
- [4] V. Scagnoli, U. Staub, Y. Bodenthin, R. A. de Souza, M. García-Fernández, M. Garganourakis, A. T. Boothroyd, D. Prabhakaran, and S. W. Lovesey, *Science* **332**, 696 (2011).
- [5] A. Widera, F. Gerber, S. Fölling, T. Gericke, O. Mandel, and I. Bloch, *Phys. Rev. Lett.* **95**, 190405 (2005).
- [6] R. Barnett, D. Petrov, M. Lukin, and E. Demler, *Phys. Rev. Lett.* **96**, 190401 (2006).
- [7] N. Syassen, D. M. Bauer, M. Lettner, D. Dietze, T. Volz, S. Dürr, and G. Rempe, *Phys. Rev. Lett.* **99**, 033201 (2007).
- [8] S. Trotzky, P. Cheinet, S. Fölling, M. Feld, U. Schnorrberger, A. M. Rey, Polkovnikov, E. A. Demler, M. D. Lukin, and I. Bloch, *Science* **319**, 295 (2008).
- [9] M. L. Wall and L. D. Carr, *New J. Phys.* **11**, 055027 (2009).
- [10] M. L. Wall and L. D. Carr, *Phys. Rev. A* **82**, 013611 (2010).
- [11] J. Schachenmayer, I. Lesanovsky, A. Micheli, and A. J. Daley, *New J. Phys.* **12**, 103044 (2010).
- [12] J. Pérez-Ríos, F. Herrera, and R. V. Krems, *New J. Phys.* **12**, 103007 (2010).
- [13] A. V. Gorshkov, S. R. Manmana, G. Chen, E. Demler, M. D. Lukin, and A. M. Rey, *Phys. Rev. A* **84**, 033619 (2011).
- [14] K. R. A. Hazzard, M. van den Worm, M. Foss-Feig, S. R. Manmana, E. G. Dalla Torre, T. Pfau, M. Kastner, and A. M. Rey, *Phys. Rev. A* **90**, 063622 (2014).
- [15] L. Chomaz, S. Baier, D. Petter, M. J. Mark, F. Wächtler, L. Santos, and F. Ferlaino, *Phys. Rev. X* **6**, 041039 (2016).
- [16] D. Jaksch, C. Bruder, J. I. Cirac, C. W. Gardiner, and P. Zoller, *Phys. Rev. Lett.* **81**, 3108 (1998).
- [17] A. Sanpera, M. Lewenstein, V. Ahufinger, B. Damski, S. De, and U. Sen, *Adv. Phys.* **56**, 243 (2007).
- [18] H. Kadau, M. Schmitt, M. Wenzel, C. Wink, T. Maier, I. Ferrier-Barbut, and T. Pfau, *Nature* **530**, 194 (2016).
- [19] N. Q. Burdick, A. G. Sykes, Y. Tang, and B. L. Lev, *New Journal of Physics* **18**, 113004 (2016).
- [20] M. Schmitt, M. Wenzel, F. Böttcher, I. Ferrier-Barbut, and T. Pfau, *Nature* **539**, 259 (2016).
- [21] L. Chomaz, R. M. W. van Bijnen, D. Petter, G. Faraoni, S. Baier, J. H. Becher, M. J. Mark, F. Wächtler, L. Santos, and F. Ferlaino, *Nature Physics* (2018), 10.1038/s41567-018-0054-7.
- [22] S. Hensler, J. Werner, A. Griesmaier, P. Schmidt, A. Görlitz, T. Pfau, S. Giovanazzi, and K. Rzazewski, *Applied Physics B* **77**, 765 (2003).
- [23] A. de Paz, A. Sharma, A. Chotia, E. Maréchal, J. H. Huckans, P. Pedri, L. Santos, O. Gorceix, L. Vernac, and B. Laburthe-Tolra, *Phys. Rev. Lett.* **111**, 185305 (2013).
- [24] D. M. Brink and G. R. Satchler, *Angular momentum*, 3rd ed. (Oxford University Press, Oxford, 1993).
- [25] A. Frisch, M. Mark, K. Aikawa, F. Ferlaino, J. L. Bohn, C. Makrides, A. Petrov, and S. Kotochigova, *Nature* **507**, 475 (2014).
- [26] T. Maier, H. Kadau, M. Schmitt, M. Wenzel, I. Ferrier-Barbut, T. Pfau, A. Frisch, S. Baier, K. Aikawa, L. Chomaz, M. J. Mark, F. Ferlaino, C. Makrides, E. Tiesinga, A. Petrov, and S. Kotochigova, *Phys. Rev. X* **5**, 041029 (2015).
- [27] Y.-J. Lin, R. L. Compton, J. V. P. K. Jiménez-García, and I. B. Spielman, *Nature* **462**, 628 (2009).
- [28] L. J. LeBlanc, K. Jiménez-García, R. A. Williams, M. C. Beeler, A. R. Perry, W. D. Phillips, and I. B. Spielman, *PNAS* **109**, 10811 (2012).
- [29] S. Kotochigova, *Rep. Prog. in Phys.* **77**, 093901 (2014).
- [30] S. Baier, M. J. Mark, D. Petter, K. Aikawa, L. Chomaz, Z. Cai, M. Baranov, P. Zoller, and F. Ferlaino, *Science* **352**, 201 (2016).
- [31] D. T. Colbert and W. H. Miller, *J. Chem. Phys.* **96**, 1982 (1992).
- [32] E. Tiesinga, C. J. Williams, and P. S. Julienne, *Phys. Rev. A* **57**, 4257 (1998).
- [33] T. Busch, B.-G. Englert, K. Rzazewski, and M. Wilkens, *Foundations of Physics* **28**, 549 (1998).
- [34] E. Tiesinga, C. J. Williams, F. H. Mies, and P. S. Julienne, *Phys. Rev. A* **61**, 063416 (2000).
- [35] C. Cohen-Tannoudji, J. Dupont-Roc, and G. Grynberg, *Atom-Photon Interactions* (Wiley-VCH, Weinheim, 2004).

- [36] G. F. Gribakin and V. V. Flambaum, *Phys. Rev. A* **48**, 546 (1993).
- [37] A. Griesmaier, J. Werner, S. Hensler, J. Stuhler, and T. Pfau, *Phys. Rev. Lett.* **94**, 160401 (2005).
- [38] J. Werner, A. Griesmaier, S. Hensler, J. Stuhler, T. Pfau, A. Simoni, and E. Tiesinga, *Phys. Rev. Lett.* **94**, 183201 (2005).
- [39] T. Lahaye, C. Menotti, L. Santos, M. Lewenstein, and T. Pfau, *Rep. Prog. Phys.* **72**, 126401 (2009).
- [40] J. Stuhler, A. Griesmaier, J. Werner, T. Koch, M. Fattori, and T. Pfau, *J. Modern Optics* **54**, 647 (2010).
- [41] A. de Paz, P. Pedri, A. Sharma, M. Efremov, B. Naylor, O. Gorceix, E. Maréchal, L. Vernac, and B. Laburthe-Tolra, *Phys. Rev. A* **93**, 021603(R) (2016).
- [42] Z. Pavlović, R. V. Krems, R. Côté, and H. R. Sadeghpour, *Phys. Rev. A* **71**, 061402(R) (2005).
- [43] M. A. Baranov, M. Dalmonte, G. Pupillo, and P. Zoller, *Chem. Rev.* **112**, 5012 (2012).